ELSEVIER

International Journal of Mass Spectrometry 222 (2003) 431–450

International Journal of Mass Spectrometry

www.elsevier.com/locate/ijms

Influence of substituents on cation–π interactions 5. Absolute binding energies of alkali metal cation–anisole complexes determined by threshold collision-induced dissociation and theoretical studies

R. Amunugama, M.T. Rodgers*

Department of Chemistry, Wayne State University, Detroit, MI 48202, USA

Received 13 May 2002; accepted 9 July 2002

In honor of J.L. Beauchamp on the occasion of his 60th birthday, in thanks for his numerous contributions to gas-phase ion chemistry, and in appreciation for his mentoring and friendship.

Abstract

Threshold collision-induced dissociation (CID) techniques are employed to determine the bond dissociation energies of cation–π complexes of anisole and the alkali metal cations. Both mono and sandwich complexes to Li^+, Na^+, K^+, Rb^+, and Cs^+ are examined. In every complex, the primary and lowest energy dissociation pathway observed is endothermic loss of an intact anisole ligand. Sequential dissociation of a second anisole ligand is observed at elevated energies in the sandwich complexes. Ligand exchange reactions to produce M^+Xe and $M^+(C_6H_5OCH_3)Xe$ are also observed as minor reaction pathways. The molecular constants necessary for the thermodynamic analysis of the experimental data as well as the structures of these complexes are determined from B3LYP/6-31G* calculations. Theoretical binding energies are determined from single point calculations at the MP2(full)/6-311+G(2d, 2p) level using the B3LYP/6-31G* optimized geometries. The agreement between theory and experiment is very good in all cases except for the $Li^+(C_6H_5OCH_3)$ complex. The trends in the bond dissociation energies of these complexes to anisole as well as those to other π ligands previously studied, aniline, benzene, fluorobenzene, phenol, and toluene, confirm that these cation–π complexes are noncovalently bound. Comparisons amongst these π ligands are made to examine the influence of the substituent on the binding, and the factors that control the strength of cation–π interactions. (Int J Mass Spectrom 222 (2003) 431–450)

Keywords: Alkali metal ions; Bond dissociation energies; Cation–π interactions; Collision-induced dissociation; Guided ion beams

1. Introduction

Cation–π interactions have become an increasingly popular topic of study among chemists, biophysicists, and biologists. These studies have been motivated by experimental evidence accumulated over the last 10 years that make it clear that cation–π interactions are operative in complex biological systems [1–14]. In biological systems such as proteins, cation–π interactions exist between a positively charged species such

* Corresponding author. E-mail: mrodgers@chem.wayne.edu

1387-3806/02/$ – see front matter
PII S1387-3806(02)00945-4

as a metal cation (e.g., Na^+ or K^+) or a protonated side chain of a basic amino acid (e.g., lysine or arginine) and the π face of an aromatic amino acid. Such cation–π interactions are believed to play a role in protein structural organization [3–10] and the functioning of ionic channels in membranes [11,12]. In addition, it is believed that cation–π interactions might also play an important role in molecular recognition processes [15,16]. Therefore, current studies of cation–π interactions are aimed at achieving both a better understanding of these interactions from a fundamental point of view as well as the specific roles they play in biological systems. Fundamental studies of cation–π interactions generally involve the examination of the association or dissociation behavior of isolated complexes of metal cations to aromatic ligands. Such gas phase studies allow the extraction of the intrinsic enthalpy or free energy of binding and thus provide a quantitative measure of the strength of the cation–π interaction. By varying the cation and π ligands under investigation, these studies seek to determine the influence that the size and electron configuration of the metal ion as well as the local environment of the π ligand has upon the cation–π interaction. Since the first thermochemical measurement of the strength of the cation–π interaction between K^+ and benzene by Kebarle and coworkers using high pressure mass spectrometry techniques [17], there have been a number of experimental [18–34] and theoretical [5,35–40] studies reported in the literature aimed at determining the strength of cation–π interactions between a variety of metal cations and aromatic ligands. These studies have examined a number of model systems [17–19,25–29,32–34] as well as the aromatic amino acids [20,21]. Amongst these model systems, benzene [17,25,26,32–34] and pyrrole [19,27], and their derivatives such as toluene [28], fluorobenzene [29], aniline [30], phenol [18,31], and indole [18] are of particular interest because they constitute the simplest groups of larger aromatic ligands that could mimic the binding properties of complex π ligands that participate in cation–π interactions operative in biological systems. Amongst these studies, a great deal of attention has been focused on cation–π interactions involving the alkali metal cations. These include Na^+ and K^+, the most biologically relevant alkali metal cations [41] as well as other alkali metal cations whose involvement in biological systems has been documented [2–4]. In the present study, we examine cation–π interactions of anisole, $C_6H_5OCH_3$, with the alkali metal cations, Li^+, Na^+, K^+, Rb^+, and Cs^+. No previous experimental investigations or theoretical studies of cation–π interactions between alkali metal cations and anisole have been reported in the literature. The structure of anisole along with its measured [42] and calculated dipole moments (determined here) and estimated polarizability [43] are shown in Fig. 1. The kinetic energy-dependent cross-sections for the collision-induced dissociation (CID) processes are analyzed using methods developed previously [44]. The analysis explicitly includes the effects of the internal and translational energy distributions of the reactants, multiple ion–neutral collisions, and the lifetime for dissociation. We derive $(C_6H_5OCH_3)_{x-1}M^+–C_6H_5OCH_3$, $x = 1–2$, bond dissociation energies (BDEs) for all of the complexes and compare these results to ab initio and density functional calculations performed here. Comparisons are also made to the analogous benzene [26], toluene [28], fluorobenzene [29], aniline [30], and phenol [31] systems studied previously to examine the influence of the methoxy substituent on the binding, and the factors that control the strength of cation–π interactions.

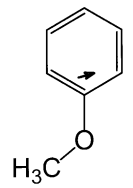

Anisole
1.38 D (1.37 D)
12.84 Å3

Fig. 1. Structure of the phenol molecule. The properly scaled dipole moment in Debeye is shown as an arrow. Values listed are taken from experiment [42] and theoretical calculations performed here (in parentheses). The estimated polarizability is also shown [43].

2. Experimental

2.1. General procedures

A guided ion beam mass spectrometer that has been described in detail previously [45] was used to measure the cross-sections for CID of $M^+(C_6H_5OCH_3)_x$ complexes, where $M^+ = Li^+$, Na^+, K^+, Rb^+, and Cs^+ and $x = 1-2$. The $M^+(C_6H_5OCH_3)_x$ complexes are generated in a flow tube ion source by condensation of the alkali metal cation and neutral anisole molecule(s). These complexes are collisionally stabilized and thermalized by $\sim 10^5$ collisions with the He and Ar bath gases such that the internal energies of the ions emanating from the source region are well described by a Maxwell–Boltzmann distribution at room temperature [45]. The ions are extracted from the source, accelerated, and focused into a magnetic sector momentum analyzer for mass analysis. Mass-selected ions are decelerated to a desired kinetic energy and focused into an octopole ion guide, which acts as an efficient ion trap in the radial direction [46]. The octopole passes through a static gas cell containing Xe at low pressures (0.05–0.20 mTorr), to ensure that multiple ion–neutral collisions are improbable. The trapping field of the octopole efficiently focuses scattered reactant and product ions. These ions drift to the end of the octopole where they are focused into a quadrupole mass filter for mass analysis and subsequently detected with a secondary electron scintillation detector and standard pulse counting techniques.

Ion intensities are converted to absolute cross-sections using a Beer's law analysis [47]. Absolute uncertainties in cross-section magnitudes are estimated to be ±20%, which are largely the result of errors in the pressure measurement and the length of the interaction region. Relative uncertainties are approximately ±5%. Because the radio frequency used for the octopole does not trap light masses with high efficiency, absolute magnitudes of the cross-sections for production of Li^+ are probably accurate to ±50%.

Ion kinetic energies in the laboratory frame, E_{lab}, are converted to energies in the center of mass frame. All energies reported below are in the CM frame unless otherwise noted. The absolute zero and distribution of the ion kinetic energies are determined using the octopole ion guide as a retarding potential analyzer as previously described [47]. The distribution of ion kinetic energies is Gaussian with a fwhm between 0.2 and 0.4 eV (lab) for these experiments. The uncertainty in the absolute energy scale is ±0.05 eV (lab).

Because multiple collisions can influence the shape of CID cross-sections and the threshold regions are most sensitive to these effects, we have performed pressure-dependent studies of all cross-sections examined here. Data free from pressure effects are obtained by extrapolating to zero reactant pressure, as described previously [48]. Thus, results reported below are due to single bimolecular encounters.

2.2. Thermochemical analysis

The threshold regions of the reaction cross-sections are modeled using Eq. (1):

$$\sigma(E) = \sigma_0 \sum_i g_i (E + E_i - E_0)^n / E \quad (1)$$

where σ_0 is an energy independent scaling factor, E is the relative translational energy of the reactants, E_0 is the threshold for reaction of the ground electronic and ro-vibrational state, and n is an adjustable parameter. The summation is over the ro-vibrational states of the reactant ions, i, where E_i is the excitation energy of each ro-vibrational state, and g_i is the population of those states ($\Sigma g_i = 1$). The populations of excited ro-vibrational levels are not negligible even at 298 K as a result of the many low-frequency modes present in these ions. The relative reactivity of all ro-vibrational states, as reflected by σ_0 and n, is assumed to be equivalent.

The Beyer–Swinehart algorithm [49] is used to evaluate the density of the ro-vibrational states, and the relative populations, g_i are calculated by an appropriate Maxwell–Boltzmann distribution at the 298 K temperature appropriated for the reactants. The vibrational frequencies of the reactant complexes are determined from density functional theory calculations as discussed in Section 2.3. The average vibrational

energy at 298 K of the $M^+(C_6H_5OCH_3)_x$ complexes is given in Table 1. To account for the inaccuracies in the calculated frequencies, we have increased and decreased the scaled calculated frequencies by 10% for the $M^+(C_6H_5OCH_3)_x$ complexes to Li^+, Na^+, and K^+. This scaling procedure encompasses the range of scale factors needed to bring calculated frequencies into agreement with experimentally determined frequencies as found by Pople et al. [50]. For the complexes to Rb^+ and Cs^+, 20% variations were applied. The corresponding change in the average vibrational energy is taken to be an estimate of one standard deviation of the uncertainty in vibrational energy (Table 1).

We also include statistical theories for unimolecular dissociation, specifically Rice–Ramsperger–Kassel–Marcus (RRKM) theory, in Eq. (1) to account for the possibility that collisionally activated ions may not have undergone dissociation prior to arriving at the detector ($\sim 10^{-4}$ s) [44,51]. The ro-vibrational frequencies appropriate for the energized molecules and the transition states (TSs) leading to dissociation are given in Tables 1 and 2. In our analysis, we assume that the TSs are loose and product-like because the interaction between the alkali metal cation and the anisole ligand(s) is largely electrostatic (ion-dipole, ion quadrupole, and ion-induced dipole interactions). The most appropriate model for the TS of such electrostatically bound complexes is a loose phase space limit (PSL) model located at the centrifugal barrier for the interaction of $M^+(C_6H_5OCH_3)_{x-1}$ with $C_6H_5OCH_3$ as described in detail elsewhere [44]. The TS vibrations appropriate for this model are the frequencies of the products, which are also found in Table 1. The transitional frequencies, those that become rotations of the completely dissociated products, are treated as rotors. The transitional mode rotors and the 1-D external rotor of the TS are simply the rotational constants of the molecular product(s) formed in the CID reaction as previously discussed in detail. These are listed in Table 2. The 2-D external rotational constant of the TS is determined by assuming that the TS occurs at the centrifugal barrier for interaction of $M^+(C_6H_5OCH_3)_{x-1}$ with the neutral $C_6H_5OCH_3$ molecule, treated variationally as outlined elsewhere [44]. The 2-D external rotations are treated adiabatically with centrifugal effects included using a statistical distribution with explicit summation over the possible values of the rotational quantum number, as described in detail elsewhere [44].

The model represented by Eq. (1) is expected to be appropriate for translationally driven reactions [52] and has been found to reproduce CID cross-sections well. The model is convoluted with the kinetic energy distributions of both reactants, and a nonlinear least-squares analysis of the data is performed to give optimized values for the parameters σ_0, E_0, and n. The error associated with the measurement of E_0 is estimated from the range of threshold values determined for different zero-pressure extrapolated data sets, variations associated with uncertainties in the vibrational frequencies, and the error in the absolute energy scale, 0.05 eV (lab). For analyses that include the RRKM lifetime analysis, the uncertainties in the reported E_0 values also include the effects of increasing and decreasing the time assumed available for dissociation ($\sim 10^{-4}$ s) by a factor of 2.

Eq. (1) explicitly includes the internal energy of the ion, E_i. All energy available is treated statistically because the internal (rotational and vibrational) energy of the reactants is redistributed throughout the ion in the collision. Because the CID processes examined here are simple noncovalent bond fission reactions, the E_0 values determined by analysis using Eq. (1) can be equated to 0 K bond dissociation energies (see, for example, Fig. 1) [53,54].

2.3. Theoretical calculations

To obtain model structures, vibrational frequencies, rotational constants, and energetics for the neutral $C_6H_5OCH_3$ ligand and for the $M^+(C_6H_5OCH_3)_x$ complexes, ab initio and density functional theory calculations were performed using Gaussian 98 [55]. Geometry optimizations were performed at B3LYP/6-31G* level [56,57] for the $M^+(C_6H_5OCH_3)_x$ complexes where $M^+ = Li^+$, Na^+, and K^+. For complexes with Rb^+ and Cs^+, geometry optimizations were performed using a hybrid basis set in

Table 1
Vibrational frequencies and average vibrational energies at 298 K[a]

Species	E_{vib} (eV)[b]	Frequencies (cm^{-1})
$C_6H_5OCH_3$	0.08 (0.02)	91, 210, 254, 275, 417, 439, 512, 550, 617, 689, 753, 787, 815, 875, 937, 963, 993, 1031, 1062, 1092, 1162, 1166, 1184, 1195, 1271, 1325, 1347, 1468, 1477, 1491, 1505, 1521, 1613, 1634, 2964, 3021, 3094, 3121, 3128, 3145, 3153, 3162
$Li^+(C_6H_5OCH_3)$	0.19 (0.02)	107, 180, 225, 240, 251, 284, 393, 420, 439, 528, 549, 612, 688, 786, 796, 864, 908, 983, 987, 995, 1014, 1029, 1081, 1154, 1169, 1181, 1190, 1293, 1319, 1341, 1455, 1466, 1491, 1495, 1512, 1569, 1604, 2999, 3074, 3139, 3151, 3155, 3166, 3172, 3177
$Na^+(C_6H_5OCH_3)$	0.21 (0.02)	78, 105, 129, 199, 209, 240, 262, 422, 437, 525, 550, 613, 694, 780, 790, 851, 898, 972, 981, 991, 1015, 1033, 1083, 1155, 1167, 1181, 1189, 1287, 1316, 1340, 1458, 1467, 1493, 1493, 1511, 1579, 1610, 2990, 3063, 3133, 3140, 3145, 3158, 3163, 3171
$K^+(C_6H_5OCH_3)$	0.21 (0.02)	57, 87, 114, 143, 202, 244, 266, 420, 437, 519, 550, 614, 688, 773, 788, 844, 893, 967, 977, 990, 1018, 1038, 1085, 1157, 1167, 1182, 1190, 1283, 1317, 1342, 1463, 1469, 1494, 1496, 1513, 1589, 1616, 2984, 3056, 3127, 3134, 3140, 3154, 3159, 3169
$Rb^+(C_6H_5OCH_3)$	0.22 (0.04)	49, 75, 114, 123, 202, 244, 266, 420, 437, 519, 550, 614, 688, 773, 788, 844, 893, 967, 977, 990, 1018, 1038, 1085, 1157, 1167, 1182, 1190, 1283, 1317, 1342, 1463, 1469, 1494, 1496, 1513, 1589, 1616, 2984, 3056, 3127, 3134, 3140, 3154, 3159, 3169
$Cs^+(C_6H_5OCH_3)$	0.22 (0.04)	47, 71, 114, 117, 202, 244, 266, 420, 437, 519, 550, 614, 688, 773, 788, 844, 893, 967, 977, 990, 1018, 1038, 1085, 1157, 1167, 1182, 1190, 1283, 1317, 1342, 1463, 1469, 1494, 1496, 1513, 1589, 1616, 2984, 3056, 3127, 3134, 3140, 3154, 3159, 3169
$Li^+(C_6H_5OCH_3)_2$	0.44 (0.04)	9, 32, 42, 61, 75, 105, 109, 120, 188, 196, 201, 215, 243, 245, 262, 265, 390, 418, 418, 438, 439, 523, 524, 550(2), 613, 614, 691(2), 782, 783, 791, 793, 850, 856, 900, 903, 976, 978, 985, 986, 991, 992, 1018(2), 1036, 1037, 1084, 1085, 1156, 1157, 1167(2), 1182, 1183, 1191(2), 1290(2), 1318, 1319, 1342, 1343, 1460, 1461, 1468, 1469, 1493, 1494, 1495, 1496, 1513, 1514, 1582, 1583, 1612, 1613, 2991(2), 3062(2), 3130(2), 3146(2), 3150, 3151, 3163, 3164, 3168(2), 3176(2)
$Na^+(C_6H_5OCH_3)_2$	0.46 (0.04)	7, 20, 28, 40, 73, 88, 95, 108, 114, 126, 197, 207, 237, 244, 245, 262, 266, 422(2), 438(2), 522, 523, 550(2), 614, 615, 694, 695, 775, 776, 789, 790, 843, 847, 895, 897, 968, 970, 980, 981, 990(2), 1018(2), 1038(2), 1084, 1085, 1157(2), 1166(2), 1182(2), 1191(2), 1285, 1286, 1317(2), 1341(2), 1461, 1462, 1468, 1469, 1493, 1494, 1495, 1496, 1513(2), 1585, 1586, 1614(2), 2986(2), 3057(2), 3127(2), 3138(2), 3143(2), 3157(2), 3162(2), 3172(2)
$K^+(C_6H_5OCH_3)_2$	0.47 (0.03)	4, 5, 7, 35, 64, 74, 80, 89, 110, 113, 163, 203, 204, 246, 247, 266(2), 419, 420, 437(2), 518(2), 550(2), 614(2), 687(2), 768, 770, 788(2), 838, 840, 889, 890, 963, 964, 975, 976, 990(2), 1020(2), 1041(2), 1086(2), 1157(2), 1166(2), 1182(2), 1190(2), 1281, 1282, 1317(2), 1343(2), 1463(2), 1469(2), 1493(2), 1497(2), 1514(2), 1591(2), 1618(2), 2981(2), 3051, 3052, 3123(2), 3133(2), 3139(2), 3153(2), 3159(2), 3169(2)
$Rb^+(C_6H_5OCH_3)_2$	0.48 (0.07)	3, 4, 6, 30, 64, 74, 80, 89, 110, 113, 140, 203, 204, 246, 247, 266(2), 419, 420, 437(2), 518(2), 550(2), 614(2), 687(2), 768, 770, 788(2), 838, 840, 889, 890, 963, 964, 975, 976, 990(2), 1020(2), 1041(2), 1086(2), 1157(2), 1166(2), 1182(2), 1190(2), 1281, 1282, 1317(2), 1343(2), 1463(2), 1469(2), 1493(2), 1497(2), 1514(2), 1591(2), 1618(2), 2981(2), 3051, 3052, 3123(2), 3133(2), 3139(2), 3153(2), 3159(2), 3169(2)
$Cs^+(C_6H_5OCH_3)_2$	0.48 (0.07)	3, 4, 6, 29, 64, 74, 80, 89, 110, 113, 134, 203, 204, 246, 247, 266(2), 419, 420, 437(2), 518(2), 550(2), 614(2), 687(2), 768, 770, 788(2), 838, 840, 889, 890, 963, 964, 975, 976, 990(2), 1020(2), 1041(2), 1086(2), 1157(2), 1166(2), 1182(2), 1190(2), 1281, 1282, 1317(2), 1343(2), 1463(2), 1469(2), 1493(2), 1497(2), 1514(2), 1591(2), 1618(2), 2981(2), 3051, 3052, 3123(2), 3133(2), 3139(2), 3153(2), 3159(2), 3169(2)

[a] Vibrational frequencies are obtained from a vibrational analysis of the density functional theory B3LYP/6-31G* geometry optimized structures for neutral $C_6H_5OCH_3$ and $M^+(C_6H_5OCH_3)_x$, where $M^+ = Li^+$, Na^+, and K^+ and scaled by 0.9804. For $M^+ = Rb^+$ and Cs^+, vibrational frequencies were estimated by scaling the calculated frequencies for the analogous $K^+(C_6H_5OCH_3)_x$ complexes as described in the text. The metal–ligand stretches and bends, corresponding to the transitional modes, are indicated in bold typeface, where the largest of these frequencies is the reaction coordinate.

[b] Uncertainties listed in parentheses are determined as described in the text.

Table 2
Rotational constants of the reactant $M^+(C_6H_5OCH_3)_x$ complexes and their transition states for collision-induced dissociation in cm^{-1}

Reactant	Energized molecule		Transition state		
	1-D[a]	2-D[b]	1-D[c]	2-D[c]	2-D[d]
$Li^+(C_6H_5OCH_3)$	0.136	0.043	0.17	0.046	0.038
$Na^+(C_6H_5OCH_3)$	0.085	0.037	0.17	0.046	0.0038
$K^+(C_6H_5OCH_3)$	0.059	0.031	0.17	0.046	0.0016
$Rb^+(C_6H_5OCH_3)$	0.059	0.031	0.17	0.046	0.0006
$Cs^+(C_6H_5OCH_3)$	0.059	0.031	0.17	0.046	0.0003
$Li^+(C_6H_5OCH_3)_2$	0.028	0.010	0.14, 0.17	0.043, 0.046	0.0012
$Na^+(C_6H_5OCH_3)_2$	0.025	0.0081	0.085, 0.17	0.037, 0.046	0.0010
$K^+(C_6H_5OCH_3)_2$	0.023	0.0066	0.059, 0.17	0.031, 0.046	0.0010
$Rb^+(C_6H_5OCH_3)_2$	0.023	0.0065	0.059, 0.17	0.031, 0.046	0.0008
$Cs^+(C_6H_5OCH_3)_2$	0.023	0.0065	0.059, 0.17	0.031, 0.046	0.0005

[a] Active external.
[b] Inactive external.
[c] Rotational constants of the transition state treated as free internal rotors.
[d] Two-dimensional rotational constant of the transition state at threshold, treated variationally and statistically.

which the effective core potentials (ECPs) and valence basis sets of Hay and Wadt were used to describe the metal cation [58], while 6-31G* basis sets were used for C, O, and H atoms. As suggested by Glendening et al. [59], a single polarization (d) function was added to the Hay–Wadt valence basis set for Rb and Cs, with exponents of 0.24 and 0.19, respectively.

Vibrational analyses of the geometry-optimized structures were performed to determine the vibrational frequencies for the neutral $C_6H_5OCH_3$ ligand and the $M^+(C_6H_5OCH_3)_x$ complexes for $M^+ = Li^+$, Na^+, and K^+. The vibrational frequencies for the complexes to Rb^+ and Cs^+ were estimated by scaling the calculated frequencies for the analogous K^+ complexes using a procedure described in detail previously [60]. When used to model data or calculate thermal energy corrections, the calculated vibrational frequencies were scaled by a factor of 0.9804 [61]. The vibrational frequencies and rotational constants of neutral $C_6H_5OCH_3$ and all 10 $M^+(C_6H_5OCH_3)_x$ complexes are listed in Tables 1 and 2, respectively. Single point energy calculations were performed at the MP2(full)/6-311+G(2d,2p) level using the B3LYP/6-31G* and B3LYP/Hybrid (6-31G*, Hay–Wadt) optimized geometries. To obtain accurate BDEs, zero-point energy (ZPE) and basis set superposition errors (BSSE) corrections were applied [62,63]. The ZPE corrections are small and decrease with increasing size of the alkali metal ion. The BSSE corrections are somewhat larger. Calculations in which the alkali metal cation interacts with the oxygen atom of methoxy group through a σ-binding interaction were also performed for the $M^+(C_6H_5OCH_3)$ complexes. Two different stable conformations were found, hereafter referred to as σ1 and σ2. In these complexes, the ZPE corrections are somewhat smaller than for the complexes in which the alkali metal cation interactions with the π electron density of the aromatic ring. The BSSE corrections for these complexes are comparable to those for the cation–π complexes.

3. Results

3.1. Cross-sections for collision-induced dissociation

Experimental cross-sections were obtained for the interaction of 10 $M^+(C_6H_5OCH_3)_x$ complexes with Xe, where $M^+ = Li^+$, Na^+, K^+, Rb^+, and Cs^+, and $x = 1$ and 2. Representative data for the $Na^+(C_6H_5OCH_3)_x$, $x = 1$ and 2 complexes are shown in Fig. 2. The behavior of the other $M^+(C_6H_5OCH_3)_x$

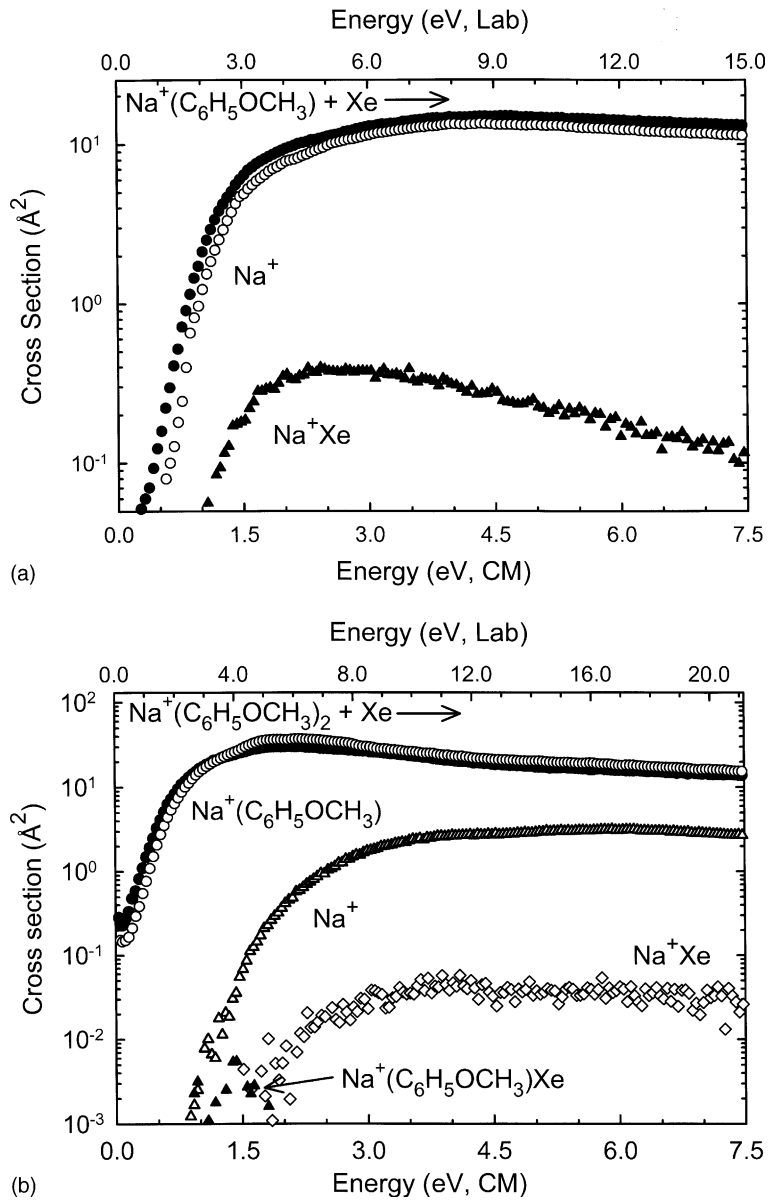

Fig. 2. Cross-sections for collision-induced dissociation of $Na^+(C_6H_5OCH_3)_x$, $x = 1$ and 2 (parts (a) and (b), respectively), with Xe as a function of kinetic energy in the center-of-mass frame (lower x-axis) and the laboratory frame (upper x-axis). Data are shown for a Xe pressure of ~0.2 and ~0.1 mTorr, for the $x = 1$ and 2 complexes, respectively. The open symbols for all $M^+(C_6H_5OH)_x$ represent data extrapolated to zero pressure. Primary and secondary product cross-sections are shown as (●) and (△), respectively. Primary and secondary ligand exchange product cross-sections are shown as (▲) and (◇), respectively. Data are also shown for the primary product cross-section extrapolated to zero pressure of Xe as (○).

complexes is quite similar to that observed for the $Na^+(C_6H_5OCH_3)_x$ complexes. Over the collision energy range studied, 0 to >5 eV, only two types of processes are observed; simple CID resulting in the loss of intact anisole molecules and ligand exchange with Xe. The dominant reaction pathway observed for all of the $M^+(C_6H_5OCH_3)_x$ complexes is the loss of a single intact anisole molecule in the CID reactions 2.

$$M^+(C_6H_5OCH_3)_x + Xe \rightarrow M^+(C_6H_5OCH_3)_{x-1} + C_6H_5OCH_3 + Xe \quad (2)$$

In the mono-complexes, the thresholds for reaction 2 decrease and the maximum cross-section increases as the size of the cation increases; behavior indicative of electrostatic binding. The $Rb^+(C_6H_5OCH_3)$ and $Cs^+(C_6H_5OCH_3)$ complexes deviate from this simple trend exhibiting cross-section maxima intermediate between that observed for the Na^+ and K^+ complexes. The $M^+(C_6H_5OCH_3)_2$ sandwich complexes exhibit similar behavior. The thresholds for reactions 2 again decrease and the maximum cross-section increases with increasing size of the cation. The $Rb^+(C_6H_5OCH_3)_2$ and $Cs^+(C_6H_5OCH_3)_2$ complexes again deviate from these simple trend, exhibiting cross-sections that are smaller than for the other alkali metal cations. The maximum cross-section for reaction 2, as well as the total cross-section, roughly doubles in magnitude from the mono to the sandwich complexes. The threshold for reaction 2 also decreases from the mono to the sandwich complexes, behavior that is again indicative of electrostatic binding. At elevated energies, sequential dissociation of a second anisole molecule is observed in the sandwich complexes. As this reaction pathway becomes energetically accessible, the cross-section for the primary CID process declines indicating that loss of both anisole ligands occurs sequentially rather than via a direct mechanism.

In addition to the CID processes, ligand exchange reactions are also observed. The apparent thresholds for the ligand exchange processes in the $M^+(C_6H_5OCH_3)_x$ complexes decrease regularly as the size of the cation increases and are smaller for the sandwich complexes than for the mono-complexes. The cross-section magnitudes of the ligand exchange products are quite small. The primary and secondary ligand exchange products are approximately 3 and 2 orders of magnitude smaller than the primary CID product, respectively.

3.2. Threshold analysis

The model of Eq. (1) was used to analyze the thresholds for reactions 2 in 10 $M^+(C_6H_5OCH_3)_x$ systems. The results of these analyses are given in Table 3 for all 10 $M^+(C_6H_5OCH_3)_x$ complexes. Representative fits using Eq. (1) for the $Na^+(C_6H_5OCH_3)_x$ complexes are shown in Fig. 3. Experimental

Table 3
Fitting parameters of Eq. (1), threshold dissociation energies at 0 K, and entropies of activation at 1000 K[a]

Reactant complex	σ_0[b]	n[b]	E_0[c] (eV)	E_0(PSL) (eV)	Kinetic shift (eV)	$\Delta S^\dagger$ (PSL) (J K^{-1} mol^{-1})
$Li^+(C_6H_5OCH_3)$	1.3 (0.1)	1.6 (0.1)	2.20 (0.21)	1.91 (0.19)	0.29	42 (2)
$Na^+(C_6H_5OCH_3)$	15.3 (1.4)	1.2 (0.1)	1.20 (0.1)	1.18 (0.06)	0.02	38 (2)
$K^+(C_6H_5OCH_3)$	23.9 (0.5)	1.2 (0.1)	0.82 (0.03)	0.81 (0.03)	0.01	34 (2)
$Rb^+(C_6H_5OCH_3)$	23.4 (0.7)	1.2 (0.1)	0.75 (0.06)	0.75 (0.04)	0.00	38 (3)
$Cs^+(C_6H_5OCH_3)$	27.9 (4.1)	1.2 (0.1)	0.69 (0.06)	0.69 (0.05)	0.00	43 (5)
$Li^+(C_6H_5OCH_3)_2$	52.6 (2.2)	1.3 (0.1)	1.60 (0.04)	1.26 (0.04)	0.34	37 (4)
$Na^+(C_6H_5OCH_3)_2$	54.6 (4.2)	1.3 (0.1)	1.06 (0.05)	0.93 (0.02)	0.13	30 (5)
$K^+(C_6H_5OCH_3)_2$	113.9 (3.5)	1.0 (0.1)	0.80 (0.07)	0.72 (0.03)	0.08	0.8 (5)
$Rb^+(C_6H_5OCH_3)_2$	77.1 (2.2)	1.1 (0.1)	0.73 (0.1)	0.66 (0.03)	0.07	3 (9)
$Cs^+(C_6H_5OCH_3)_2$	57.2 (2.6)	1.3 (0.1)	0.68 (0.1)	0.64 (0.06)	0.04	7 (9)

[a] Uncertainties are listed in parentheses.
[b] Average values for loose PSL transition state.
[c] No RRKM analysis.

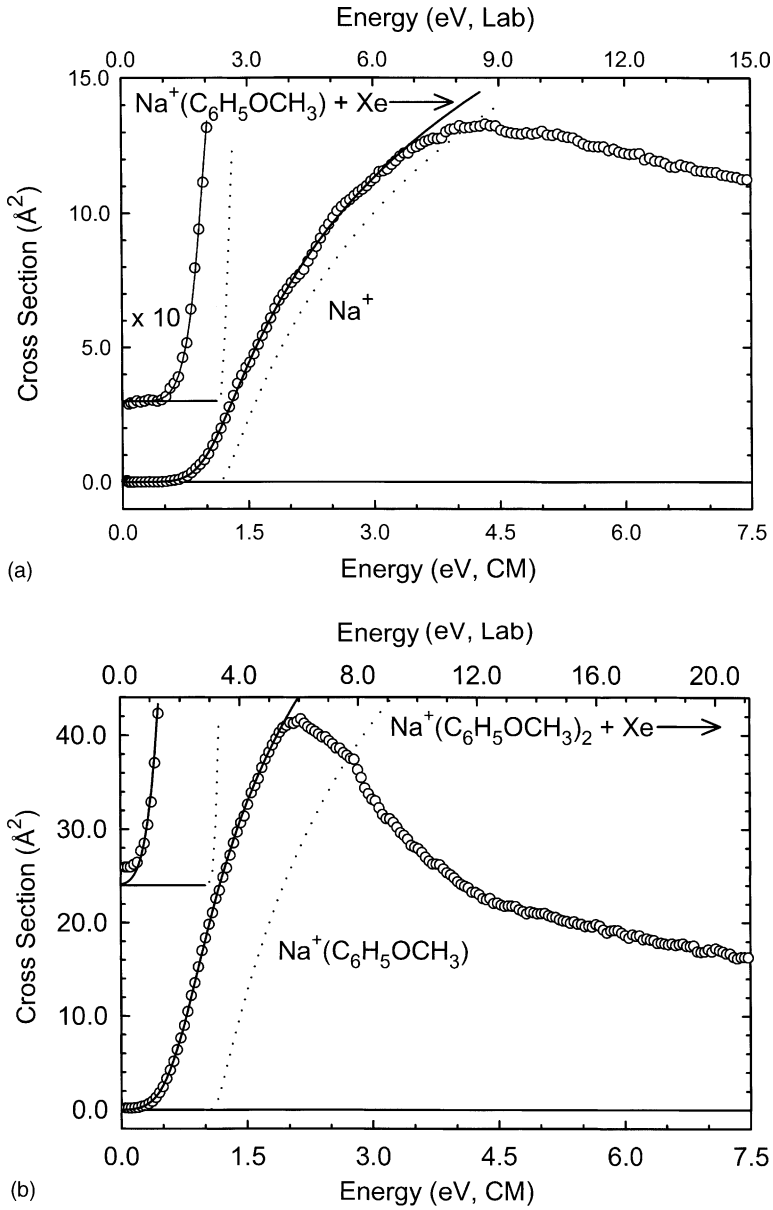

Fig. 3. Zero-pressure extrapolated cross-sections for the primary collision-induced dissociation product of the $Na^+(C_6H_5OCH_3)_x$ complexes, $x = 1$ and 2 (parts (a) and (b), respectively), with Xe in the threshold region as a function of kinetic energy in the center-of mass frame (lower x-axis) and the laboratory frame (upper x-axis). Solid lines show the best fits to the data using the model of Eq. (1) convoluted over the neutral and ion kinetic and internal energy distributions. Dashed lines show the model cross-sections in the absence of experimental kinetic energy broadening for reactants with an internal energy of 0 K.

cross-sections for the primary dissociation processes of the $M^+(C_6H_5OCH_3)_x$ complexes are accurately reproduced using a loose PSL TS model [44]. This model has been shown to provide the most accurate determination of kinetic shifts for CID reactions for electrostatically bound metal–ligand complexes [44,64]. The data are accurately reproduced over energy ranges exceeding 1 eV and over cross-section magnitudes of a factor of at least 100 for all complexes except $Rb^+(C_6H_5OCH_3)_2$ and $Cs^+(C_6H_5OCH_3)_2$ because the cross-sections for the primary product are already nonzero at 0 eV in these complexes. Threshold values, E_0(PSL) and E_0, obtained from analyses of the data with and without explicit consideration of lifetime effects are also included in Table 3. The difference between these threshold values, the kinetic shift, is also given in Table 3. The kinetic shifts observed for these systems vary from 0.0 to 0.25 eV for the mono-complexes which possess 45 vibrational modes, and from 0.04 to 0.34 eV for the sandwich complexes which have 93 vibrational modes. The kinetic shifts decrease with increasing size of the cation, from Li^+ to Cs^+, in both the mono and sandwich complexes. This is easily understood because the observed kinetic shift should directly correlate with the density of states of the complex at threshold, which depends upon the measured BDE as observed (Table 3).

The entropy of activation, $\Delta S^{\dagger}$, is a measure of the looseness of the transition state. It is also a reflection of the complexity of the system because it is largely determined by the molecular parameters used to model the energized molecule and the TS, but also depends upon the threshold energy. The $\Delta S^{\dagger}$(PSL) values at 1000 K are listed in Table 3 and vary between 1 and 43 $J\,K^{-1}\,mol^{-1}$. These entropies of activation compare favorably to an expanding range of noncovalently bound metal–ligand complexes previously measured in our laboratory and to those collected by Lifshitz for simple bond cleavage reactions of ions [65].

3.3. Theoretical results

Theoretical structures for neutral $C_6H_5OCH_3$ and for the $M^+(C_6H_5OCH_3)_x$ complexes, where $M^+ = Li^+$, Na^+, K^+, Rb^+, and Cs^+ and $x = 1$ and 2, were calculated as described above. Details of the geometry-optimized structures for each of these species are given in Table 4. The most stable structures for the $Na^+(C_6H_5OCH_3)$ and $Na^+(C_6H_5OCH_3)_2$ complexes are shown in Fig. 4. The metal cation binds to the π cloud of the aromatic ring of the anisole molecule, a cation–π interaction. The distortion of the anisole molecule that occurs upon complexation to the alkali metal cation is minor. The change in geometry is largest for Li^+ and decreases with increasing size of the metal cation. As summarized in Table 4, the ring C–O bond distance decreases by 0.010–0.031 Å upon complexation to the alkali metal cation. Similar behavior was observed in the analogous fluorobenzene [29], aniline [30], and phenol [31] complexes. Thus complexation to the alkali metal cation results in the ring C–X bond taking on more double bond character. The influence of alkali metal cation complexation is larger for the mono-complexes than for the sandwich complexes, and decreases in magnitude with increasing size of the alkali metal cation. The M^+–C and M^+–ring-centroid distances [66] increase

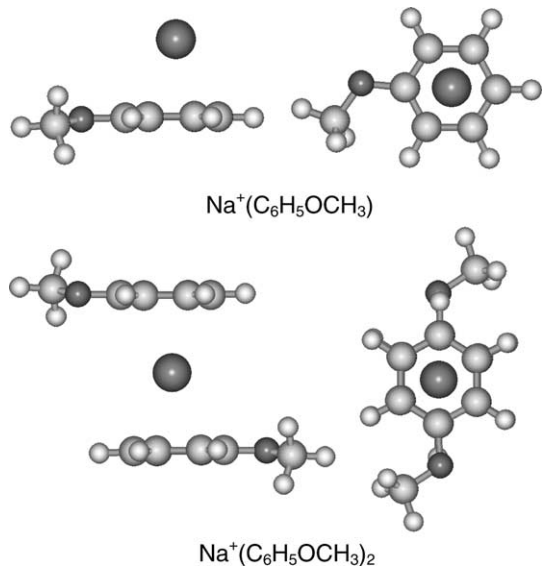

Fig. 4. B3LYP/6-31G* optimized geometries of the ground state $Na^+(C_6H_5OCH_3)_x$ cation–π complexes, where $x = 1$–2. Two views of each optimized structure are shown.

Table 4
Geometrical parameters of the B3LYP/6-31G* optimized structures of the $M^+(C_6H_5OCH_3)_x$ complexes

Complex	Conformer	M–C (Å)	M–centroid[a] (Å)	M^+–O (Å)	∠M^+OC1C6[b] (°)	∠MeOC1C2[c] (°)	C–C (Å)	C–H (Å)	CH OOP∠[d] (°)	C–O[e] (Å)	O–C[f] (Å)	C–H[g] (Å)
$C_6H_5OCH_3$							1.397	1.090	0.000	1.367	1.418	1.096
$Li^+(C_6H_5OCH_3)$	π	2.347	2.016				1.409	1.090	0.980	1.336	1.439	1.093
	σ1			1.807	88.2	91.8	1.397	1.090	0.537	1.420	1.455	1.092
	σ2			1.852	52.2	34.4	1.398	1.090	2.048	1.406	1.451	1.092
$Na^+(C_6H_5OCH_3)$	π	2.756	2.367				1.406	1.090	0.769	1.344	1.435	1.094
	σ1			2.185	88.1	91.9	1.397	1.090	0.542	1.410	1.449	1.092
	σ2			2.239	55.6	35.6	1.398	1.090	1.807	1.398	1.446	1.091
$K^+(C_6H_5OCH_3)$	π	3.186	2.749				1.404	1.090	0.698	1.351	1.432	1.094
	σ1			2.595	88.0	92.0	1.398	1.090	0.486	1.402	1.446	1.093
	σ2			2.655	63.4	37.9	1.398	1.090	1.324	1.392	1.442	1.093
$Rb^+(C_6H_5OCH_3)$[h]	π	3.464	2.989				1.403	1.090	0.602	1.354	1.430	1.094
	σ1			2.844	88.1	91.6	1.398	1.090	0.426	1.398	1.443	1.094
	σ2			2.918	65.0	34.4	1.398	1.090	1.178	1.388	1.438	1.094
$Cs^+(C_6H_5OCH_3)$[h]	π	3.720	3.218				1.402	1.090	0.482	1.357	1.428	1.095
	σ1			3.088	88.2	91.7	1.398	1.090	0.385	1.396	1.441	1.094
	σ2			3.184	68.5	32.9	1.398	1.090	0.959	1.384	1.435	1.094
$Li^+(C_6H_5OCH_3)_2$	π	2.464	2.051				1.405	1.090	0.645	1.344	1.433	1.094
$Na^+(C_6H_5OCH_3)_2$	π	2.822	2.449				1.405	1.090	0.599	1.348	1.432	1.094
$K^+(C_6H_5OCH_3)_2$	π	3.232	2.763				1.404	1.090	0.540	1.353	1.430	1.094
$Rb^+(C_6H_5OCH_3)_2$[h]	π	3.499	3.206				1.403	1.090	0.417	1.355	1.428	1.095
$Cs^+(C_6H_5OCH_3)_2$[h]	π	3.755	3.484				1.402	1.090	0.349	1.357	1.427	1.095

[a] The metal ring–centroid distance is defined as the distance from the metal atom to the central point within the aromatic ring of aniline that is in the plane of the carbon atoms.

[b] Dihedral angle.

[c] Dihedral angle.

[d] Out-of-plane angle.

[e] Ring C–O bond distance.

[f] Methyl C–O bond distance.

[g] Methyl C–H bond distance.

[h] The Hay–Wadt ECP/valence basis set was used for the metal ion, as described in the text, and the 6-31G* basis set for C and H.

with increasing size of the metal cation for both the mono and sandwich complexes. These distances are also found to increase on going from the mono to the corresponding sandwich complex.

As can be seen in Fig. 4, the ground state structure of $Na^+(C_6H_5OCH_3)$ has the Na^+ ion interacting with the π cloud of the aromatic ring such that it sits very close to the center of the ring. However, it is also possible that the alkali metal cation might interact with the lone pairs of electrons on the oxygen atom of the methoxy substituent. Two different stable conformers (σ1 and σ2) in which the alkali metal cation interacts with the methoxy substituent were found for the $M^+(C_6H_5OCH_3)$ complexes with all five alkali metal cations. The primary difference between the σ1 and σ2 conformers is the M^+–O bond distance and the orientation of the M^+–OCH_3 moiety relative to the aromatic ring. The optimized structures of the σ1 and σ2 conformers of the $Na^+(C_6H_5OCH_3)$ complex are shown in Fig. 5. In all of the σ1 conformers, the M^+–O bond distance is shorter than that found for the corresponding σ2 conformer. In the σ1 conformers, the methoxy group rotates out of the plane of the aromatic ring to allow the alkali metal cation to sit almost directly above the oxygen atom such that the ∠M^+OC1C2 and ∠MeOC1C2 dihedral angles are both close to 90°. The σ2 conformers are very similar to those found for the analogous phenol complexes. In these complexes the rotation of the substituent out of the plane is much smaller such that the ∠MeOC1C2 dihedral angles are ∼35°, and the alkali metal cation is oriented above and to the side of the substituent oxygen atom such that the ∠M^+OC1C2 dihedral angles are ∼60°. In order to understand why two different σ-binding conformers are found for anisole, whereas only one was found for phenol, we compared the energies of these ligands in their ground state configurations to those where the substituent is rotated in the same fashion as observed in the σ1 conformers, i.e., nearly perpendicular to the plane of the aromatic ring. The energetic cost of this rotation is only 2.7 kJ mol^{-1} in anisole; whereas it is somewhat higher in phenol, 16.0 kJ mol^{-1}. Thus, the repulsive interactions between the hydroxyl H atom and the aromatic ring are greater than between the methyl group and the aromatic ring. This makes the σ1 conformation in which the plane containing the M^+–OH moiety is perpendicular to the aromatic ring less favorable and not a local minimum on the potential energy surface. The σ-binding conformers of $M^+(C_6H_5OCH_3)$ and $M^+(C_6H_5OH)$ also differ from that observed for the corresponding $M^+(C_6H_5NH_2)$ complexes where the alkali metal cation sits above the C–N bond rather than directly above the N atom, making it seem appropriate to also think of these $M^+(C_6H_5NH_2)$ conformers as cation–π complexes.

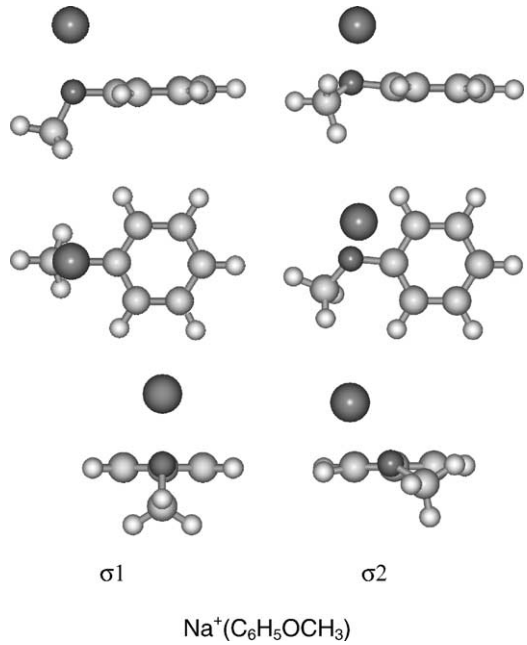

Fig. 5. B3LYP/6-31G* optimized geometries of σ-binding conformers of $Na^+(C_6H_5OCH_3)$ complex, three views of each σ-binding conformer, σ1 (1.7 kJ mol^{-1}) and σ2 (1.9 kJ mol^{-1}) are shown. Energies are relative to the ground state conformer shown in Fig. 4.

The alkali metal cation exerts a lesser influence on the aromatic ring and a greater influence on the methoxy substituent in the σ-binding complexes than in the cation–π complexes as might be expected. In contrast to that observed for the cation–π complexes, the ring C–O bond distance increases by 0.029–0.053 Å for the σ1 conformers

and by 0.017–0.039 Å for the σ2 conformers. At the MP2(full)/6-311+G(2d,2p) level of theory, the σ1 conformers of Li^+, Na^+, and K^+ are found to be 9.2, 1.7, and 2.6 kJ mol^{-1} less stable than the analogous cation–π ground state conformers, respectively. The σ2 conformers are found to be 8.5, 1.9, and 4.1 less stable than the corresponding cation–π ground state conformers, respectively. In contrast, the σ1 conformers of the Rb^+ and Cs^+ complexes are found to be 0.9 and 1.5 kJ mol^{-1} more stable than the corresponding cation–π complexes. The σ2 conformers of the Rb^+ and Cs^+ complexes are found to be less stable than the corresponding cation–π complexes by 0.8 and 1.4 kJ mol^{-1}, respectively. The small difference in stability of σ-binding and cation–π complexes suggests that the ion beams generated in our experiments are likely to be composed of a mixture of all three conformers. Because the technique employed here to determine the BDEs of these complexes is a threshold technique, our results should correlate with the least strongly bound conformer present in reasonable abundance. The population of the σ-binding conformers of the $Li^+(C_6H_5OCH_3)$ complex should be very small and are therefore unlikely to significantly influence the threshold determination.

As can be seen in Fig. 4, the lowest energy structure for the $Na^+(C_6H_5OCH_3)_2$ complex has the Na^+ cation interacting with the π clouds of the aromatic rings and has the methoxy substituents oriented anti to one another to minimize repulsive ligand–ligand interactions associated with the methoxy substituents. The anti configuration was found to be the lowest energy structure for all of the sandwich complexes. To estimate the barrier to free rotation of the aromatic ring in the sandwich complexes, optimizations were also performed for $Li^+(C_6H_5OCH_3)_2$ with the methoxy groups oriented *syn*, "*ortho*" and "*meta*" to one another. These complexes were found to be 4.7, 4.5, and 3.0 kJ mol^{-1} less stable than when oriented anti to one another (excluding BSSE corrections). Therefore, at room temperature these complexes should have sufficient energy to freely interconvert (see Table 1).

Theoretical estimates for the $M^+(C_6H_5OCH_3)_x$ BDEs were determined using the B3LYP/6-31G* geometries and single point energy calculations at both the MP2(full)/6-311+G(2d,2p) level of theory. In earlier work in which we measured and calculated the strength of cation–π interactions of $M^+(C_6H_5CH_3)_x$ complexes [28], we found better correlation between theoretical and experimental results for energetics based on MP2(full)/6-311+G(2d,2p) theory than for B3LYP/6-311+G(2d,2p) theory and have therefore employed the former in the present work. To obtain accurate BDEs, ZPE and BSSE corrections are also included. These results are listed in Table 5 along with the experimental determinations performed here for anisole.

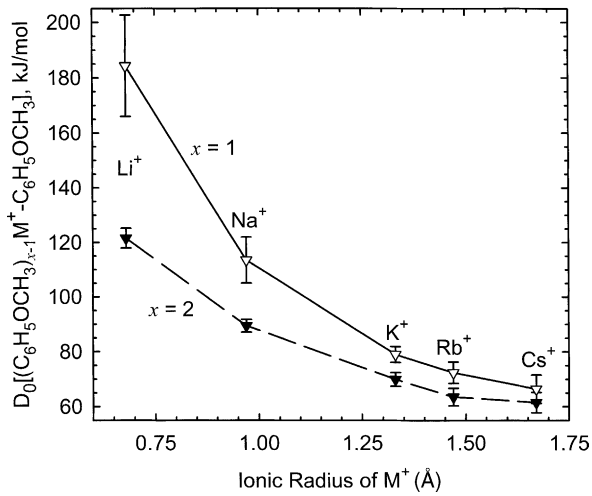

Fig. 6. Bond dissociation energies at 0 K (in kJ mol^{-1}) of the $M^+(C_6H_5OCH_3)_x$ complexes plotted versus the ionic radius of M^+. Data are shown for $x = 1$ and 2 as (▽) and (▼), respectively. All values are taken from Table 5.

4. Discussion

4.1. Trends in experimental $M^+(C_6H_5OCH_3)_x$ bond dissociation energies

The experimental BDEs of the $M^+(C_6H_5OCH_3)_x$ complexes at 0 K are summarized in Table 5. The variation in the measured BDEs with the size of the alkali metal cation is shown in Fig. 6 for both the mono and sandwich complexes. The M^+–$(C_6H_5OCH_3)$ and

Table 5
Bond dissociation enthalpies of $M^+(C_6H_5OCH_3)_x$ $x = 1$–2 at 0 K in kJ mol^{-1}

Complex	Experiment (TCID)		Theory, X = OCH_{3vv}			
	X = OCH_3[a]	X = H[b]	Conformer	D_e[c]	D_0[c,d]	$D_{0,BSSE}$[c,e]
$Li^+(C_6H_5X)$	184.4 (18.3)	161.1 (13.5)	π	174.3	167.5	157.3
			σ1	161.9	158.4	148.1
			σ2	161.6	157.3	148.8
$Na^+(C_6H_5X)$	113.5 (8.4)	92.6 (5.8)	π	114.1	110.8	100.3
		88.3 (4.3)[f]	π			
			σ1	110.3	109.0	98.6
			σ2	109.6	107.7	98.4
$K^+(C_6H_5X)$	79.0 (2.9)	73.3 (3.8)	π	88.3	85.8	79.8
			σ1	83.9	83.3	77.2
			σ2	82.5	81.3	75.7
$Rb^+(C_6H_5X)$[g]	72.4 (3.9)	68.5 (3.8)	π	73.2	71.2	64.3
			σ1	72.4	72.1	65.2
			σ2	71.2	70.2	63.5
$Cs^+(C_6H_5X)$[g]	66.4 (5.2)	64.6 (4.8)	π	65.4	63.7	57.0
			σ1	65.4	65.3	58.5
			σ2	63.3	62.6	55.6
$Li^+(C_6H_5X)_2$	121.6 (3.6)	104.2 (6.8)	π	138.1	135.4	113.4
$Na^+(C_6H_5X)_2$	89.4 (2.3)	80.0 (5.8)	π	103.3	100.5	84.7
$K^+(C_6H_5X)_2$	69.9 (2.5)	67.5 (6.8)	π	80.6	78.8	68.3
$Rb^+(C_6H_5X)_2$[g]	63.5 (3.2)	62.7 (7.7)	π	72.8	71.0	60.2
$Cs^+(C_6H_5X)_2$[g]	61.5 (3.7)	58.8 (7.7)	π	63.4	61.6	52.3

[a] Present results. Uncertainties are listed in parenthesis.
[b] Taken from Amicangelo and Armentrout, except noted [26].
[c] Calculated at the MP2(full)/6-311+G(2d,2p) level of theory using B3LYP/-31G* optimized geometries.
[d] Including zero-point energy corrections with B3LYP/6-31G* frequencies scaled by 0.9804.
[e] Also includes basis set superposition error corrections.
[f] Taken from Armentrout and Rodgers [25].
[g] The Hay–Wadt ECP/valence basis set was used for the metal ion, as described in the text.

$(C_6H_5OCH_3)M^+$–$(C_6H_5OCH_3)$ BDEs are found to decrease monotonically as the size of the alkali metal increases from Li^+ to Cs^+. Similar trends were observed for the analogous complexes to other aromatic ligands [26,28–31]. This behavior supports the conclusion that the binding in these cation–π complexes results primarily from electrostatic interactions [3]. The BDE decreases with increasing size of the alkali metal cation because the metal–ligand bond distances are larger (see Table 4) and the electrostatic interactions fall off rapidly as R^{-2} for ion–dipole, as R^{-3} for the ion–quadrupole, and as R^{-4} for ion-induced dipole interactions.

The BDEs of the sandwich complexes are smaller than the BDEs for the corresponding mono-complexes in all cases. The decrease in the measured BDE on going from the mono to the sandwich complex is largest for Li^+, and decreases with increasing size of the alkali metal cation. The sequential BDE is observed to decrease by 43.9, 15.6, 4.9, 4.4, and 4.7 kJ mol^{-1} for the Li^+, Na^+, K^+, Rb^+, and Cs^+ systems, respectively. Similar trends were observed for the analogous cation–π complexes to other aromatic ligands [26,28–31] systems. This trend is believed to be the result of Coulombic and dipole–dipole repulsions between the ligands [64]. The distance between the aromatic rings is found to increase with increasing size of the alkali metal cation, from ∼4.1 Å in $Li^+(C_6H_5OCH_3)_2$ to 6.968 Å in $Cs^+(C_6H_5OCH_3)_2$ (Table 4, 2 × M^+-centroid distance). The magnitude of the repulsive ligand–ligand interactions decreases with increasing separation of the ligands. Thus, the

differences in the BDEs for the mono and sandwich complexes decrease with increasing size of the alkali metal cation as observed. The small and similar differences observed for the K^+, Rb^+, and Cs^+ systems suggest that the ligands are distant enough to make the ligand–ligand repulsions minor and very similar for these complexes.

4.2. Comparison of theory and experiment

The experimentally determined and theoretically calculated $M^+(C_6H_5OCH_3)_x$ BDEs are listed in Table 5. The agreement between the experimental and theoretical BDEs determined at the MP2(full)/6-311+G(2d,2p)//B3LYP/6-31G* level is illustrated in Fig. 7. The mean absolute deviation (MAD) between the experimental and theoretical values for all 10 complexes is $8.6 \pm 7.6\,kJ\,mol^{-1}$ [67]. This is somewhat greater than the average experimental error of $5.4 \pm 4.9\,kJ\,mol^{-1}$. The MAD is larger for the $M^+(C_6H_5OCH_3)$ complexes, $11.7 \pm 9.7\,kJ\,mol^{-1}$, than for the $M^+(C_6H_5OCH_3)_2$ complexes, $5.4 \pm 3.2\,kJ\,mol^{-1}$. The agreement between the experimental and the six theoretical $M^+(C_6H_5OCH_3)_x$ BDEs calculated including all electrons ($M^+ = Li^+$, Na^+, K^+, $x = 1$ and 2) is reasonably good, with a MAD of $9.3 \pm 9.9\,kJ\,mol^{-1}$. These differences are somewhat larger than the average experimental error in these values of $6.3 \pm 6.3\,kJ\,mol^{-1}$. The principal contributor to the MAD for these complexes is clearly the Li^+ complex. The poorer agreement between theory and experiment for $Li^+(C_6H_5OCH_3)$ may arise for two reasons: the experimental difficulty associated with efficient detection of Li^+ [45], and the possibility that theory may systematically underestimate the bond energies for Li^+ complexes as a result of the higher degree of covalency in the metal–ligand bond. The calculated partial charge on M^+ is 0.79*e* for $Li^+(C_6H_5OCH_3)$ and varies between 0.90 and 0.99*e* for all of the other $M^+(C_6H_5OCH_3)_x$ complexes at the MP2(full)/6-311+G(2d,2p) level, indicating that the metal–ligand interaction has more covalency in the complex to Li^+ than to the other alkali metal cations. Higher levels of theory may be required to accurately describe the binding in this complex, a conclusion also drawn for Li^+ complexes with a variety of other ligands [27–31,45]. If the $Li^+(C_6H_5OCH_3)$ complex is not included, the MAD drops to $5.7 \pm 5.1\,kJ\,mol^{-1}$ and the average experimental error decreases to $3.9 \pm 2.5\,kJ\,mol^{-1}$.

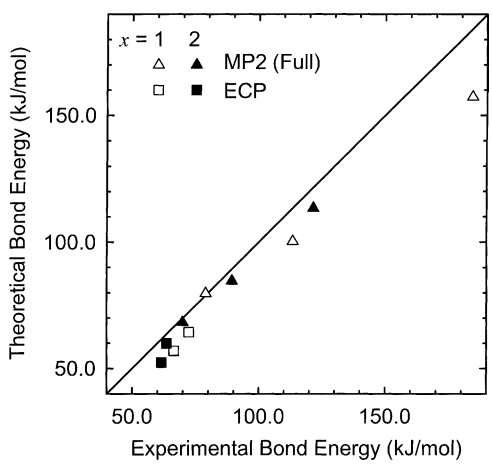

Fig. 7. Theoretical versus experimental bond dissociation energies at 0 K (in $kJ\,mol^{-1}$) of the $M^+(C_6H_5OCH_3)_x$ complexes. The diagonal line indicates the values for which the calculated and measured bond dissociation energies are equal. All values are taken from Table 5.

The agreement between the experimental and theoretical BDEs calculated using the Hay–Wadt ECP/valence basis set for the Rb^+ and Cs^+ complexes is surprisingly good. A MAD of $7.5 \pm 2.9\,kJ\,mol^{-1}$ is found. This is slightly larger than the average experimental error in these values $4.0 \pm 0.9\,kJ\,mol^{-1}$. Consistent with the analogous cation–π complexes to other aromatic ligands [26,28–31] systems, the Hay–Wadt ECP/valence basis set results in calculated BDEs that are reasonably accurate, but systematically lower than the experimental values.

4.3. Conversion from 0 to 298 K

The 0 K bond energies determined here are converted to 298 K bond enthalpies and free energies to allow comparison to commonly used experimental conditions. The enthalpy and entropy conversions are calculated using standard formulas (assuming

Table 6
Enthalpies and free energies of alkali metal cation binding of $M^+(C_6H_5OCH_3)_x$ $x = 1$–2 at 298 K in kJ mol^{-1}[a]

Reactant complex	ΔH_0[b]	$\Delta H_{298}-\Delta H_0$[c]	ΔH_{298}	$T\Delta S_{298}$[c]	ΔG_{298}
$Li^+(C_6H_5OCH_3)$	184.4 (18.3)	2.8 (2.4)	187.2 (18.5)	33.4 (7.2)	153.8 (19.8)
$Na^+(C_6H_5OCH_3)$	113.5 (8.4)	1.0 (2.0)	114.5 (8.7)	31.0 (7.6)	83.5 (11.5)
$K^+(C_6H_5OCH_3)$	79.0 (2.9)	0.4 (1.7)	79.4 (3.3)	29.2 (7.7)	50.2 (8.4)
$Rb^+(C_6H_5OCH_3)$	72.4 (3.9)	0.2 (2.0)	72.6 (4.4)	30.0 (8.1)	42.6 (9.2)
$Cs^+(C_6H_5OCH_3)$	66.4 (5.2)	0.2 (2.0)	66.6 (5.6)	30.8 (8.6)	35.8 (10.2)
$Li^+(C_6H_5OCH_3)_2$	121.6 (3.6)	−3.1 (1.8)	118.5 (4.0)	37.7 (13.4)	80.8 (13.9)
$Na^+(C_6H_5OCH_3)_2$	89.4 (2.3)	−3.2 (1.5)	86.2 (2.8)	35.4 (13.4)	50.8 (13.6)
$K^+(C_6H_5OCH_3)_2$	69.9 (2.5)	−3.6 (1.4)	66.3 (2.9)	27.0 (13.3)	39.4 (13.6)
$Rb^+(C_6H_5OCH_3)_2$	63.5 (3.2)	−3.6 (1.3)	59.9 (3.5)	27.4 (14.9)	32.5 (15.3)
$Cs^+(C_6H_5OCH_3)_2$	61.5 (3.7)	−3.6 (1.4)	57.9 (4.0)	28.2 (14.9)	29.7 (15.4)

[a] Uncertainties are listed in parentheses.
[b] Present experimental results (Table 5).
[c] Density functional values from calculations at the B3LYP/6-31G* level of theory with frequencies scaled by 0.9804. The Hay–Wadt ECP/valence basis set was used for Rb^+ and Cs^+.

harmonic oscillator and rigid rotor models) and the vibrational and rotational constants determined for the B3LYP/6-31G* optimized geometries, which are given in Tables 1 and 2. Table 6 lists 0 and 298 K enthalpies, free energies, and enthalpic and entropic corrections for all systems experimentally determined (from Table 5). The uncertainties in the enthalpic and entropic corrections are determined by 10% variation in the molecular constants for complexes to Li^+, Na^+, and K^+, and by 20% variation in the molecular constants for complexes to Rb^+ and Cs^+. Because the metal-ligand frequencies are very low and may not be adequately described by theory, the listed uncertainties also include contributions from scaling these frequencies up and down by a factor of 2. The latter provides a conservative estimate of the computational errors in these low frequency modes and is the dominant source of the uncertainties listed.

4.4. Influence of the methoxy substituent

The effect of the methoxy substituent on the cation–π interaction can be examined by comparing the results obtained here for anisole, $C_6H_5OCH_3$, to those obtained in earlier studies for benzene [26], toluene [28], fluorobenzene [29], aniline [30], and phenol [31]. In these earlier studies, it was found that the influence of the substituent on the strength of the cation–π interaction could be understood by considering the change in the quadrupole moment and polarizability of the aromatic ligand induced by the substituent. In all of the cation–π complexes studied to date, except those to aniline, the dipole moment of the aromatic ligand lies in the plane of the aromatic ring and therefore an effective interaction of the alkali metal cation with the dipole moment is not possible.

As can be seen in Fig. 8, the methoxy substituent results in an increase in the strength of the cation–π interaction as compared to benzene. This enhancement in the cation–π interaction can be understood by examining the influence of the methoxy substituent on the dipole moment, quadrupole moment, and polarizability. Benzene possesses a center of symmetry and therefore has no permanent dipole moment. Methoxy substitution eliminates the center of symmetry and results in a dipole moment of 1.38 ± 0.07 D [42]. This measured value is in good agreement with the value calculated here, 1.37 D. However, as for toluene, fluorobenzene, and phenol, the dipole moment lies in the plane of the aromatic ring. Therefore, the ion–dipole interaction should have little or no effect on the strength of the binding in the cation–π complexes to anisole. The delocalized π electron density above and below the plane of the aromatic ring produces

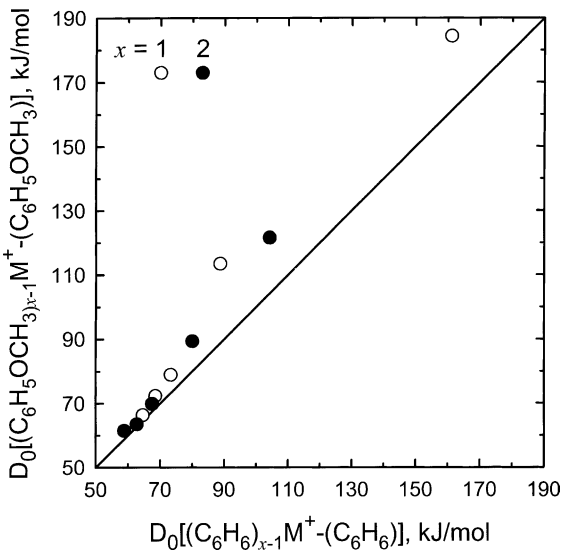

Fig. 8. Experimental bond dissociation energies (in kJ mol^{-1}) at 0 K of the $(C_6H_5OCH_3)_{x-1}M^+$–$(C_6H_5OCH_3)$ vs. $(C_6H_6)_{x-1}M^+$–(C_6H_6), where $M^+ = Li^+$, Na^+, K^+, Rb^+, and Cs^+ and $x = 1$ (○) and 2 (●). Values for C_6H_6 are taken from Amicangelo and Armentrout [26].

a quadrupole moment for benzene of −8.69 D Å [68]. The quadrupole moment however, can only be measured for molecules that have no permanent dipole moment. An estimate of the influence of the methoxy substituent on the quadrupole moment of the aromatic ring can be obtained by considering the inductive effects of the substituent. Methoxy substituents are known to have both electron donating (mesomeric) and electron withdrawing (inductive) effects on the aromatic ring. The mesomeric effect is somewhat greater than the inductive effect for anisole resulting in a small increase in the electron density of the aromatic π system. The mesomeric effect arises from one of the lone pairs of electrons on the O atom being partially delocalized over the aromatic ring as shown in the Lewis structures of anisole below.

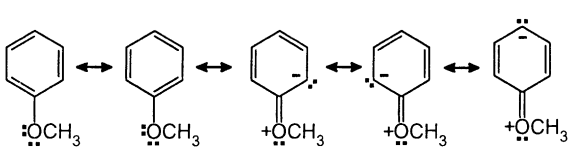

The latter three resonance structures are less favorable than the first two structures because oxygen is quite electronegative, but the electron donating properties of the methyl group help to stabilize the partial positive charge on the O atom. The delocalization of electron density into the ring results in the C–O bond taking on partial double bond character; the C–O bond distance in anisole is ∼0.05 Å shorter than that found in aliphatic alcohols such as methanol and ethanol. Therefore, a small increase in the quadrupole moment and the strength of the cation–π interaction occurs upon methoxy substitution. The polarizability of benzene is estimated using the additivity method of Miller [43] to be 9.99 Å^3 and increases to 12.84 Å^3 for anisole. Therefore the ion-induced dipole interaction should result in stronger binding to anisole compared to that observed for benzene. As discussed above, a cation–π interaction between an alkali metal cation and an aromatic ligand is expected to be largely electrostatic, arising from ion–dipole, ion–quadrupole, and ion-induced dipole interactions, but dominated by the ion–quadrupole interaction. The ion–quadrupole and ion-induced dipole effects act in concert to increase the strength of the cation–π interaction in the anisole complexes. The increase in the cation–π BDEs to anisole, relative to those of benzene, varies between 1.8 and 23.3 kJ mol^{-1} for the mono-complexes and 0.8–17.4 for the sandwich complexes. The enhancement in the binding energy is greatest for the Li^+ complexes and decreases with increasing size of the cation. Likewise, the enhancement in binding is greater for the mono-complexes than for the sandwich complexes for Li^+, Na^+, and K^+, but is slightly smaller for Rb^+ and Cs^+.

4.5. σ-Binding vs. cation–π complexes

As discussed in Section 2.3, σ-binding conformers are also found for these systems. The relative stabilities of the σ-binding vs. cation–π complexes is such that at 298 K, the temperature of the reactant ions, the distribution of ions created in our source is probably a mixture of all three conformers (π, σ1, and σ2) for all metal cations. The relative populations of the

σ-binding complexes for the $Li^+(C_6H_5OCH_3)_x$ complexes is probably quite small and <3%. The small population of the σ-binding conformers that may be present would tend to lower the measured threshold for the CID of these complexes. However, this effect should be very small for the $Li^+(C_6H_5OCH_3)_x$ systems because the population of the σ-binding conformers is expected to be quite small. The ground states of the $Na^+(C_6H_5OCH_3)$ and $K^+(C_6H_5OCH_3)$ complexes are also cation–π complexes. However, these conformers are only favored by 1.7 and 2.6 kJ mol^{-1} over the σ1 conformer, and by 1.9 and 4.1 kJ mol^{-1} over the σ2 conformer, respectively. This suggests that at 298 K only about 51 and 65% of the ions are likely to be the cation–π complexes, respectively. In contrast, the calculations find that the ground states of the $Rb^+(C_6H_5OCH_3)$ and $Cs^+(C_6H_5OCH_3)$ complexes are σ-binding conformers. The σ1 conformers are more stable than the cation–π conformers by 0.9 and 1.5 kJ mol^{-1}, and more stable than the σ2 conformers by 1.7 and 2.9 kJ mol^{-1}, respectively. This suggests that only about 32 and 29% of the ions are likely to be the cation–π complexes at 298 K, respectively. However, because the binding energies of the σ-binding and cation–π complexes are very nearly equal for all but the Li^+ systems, the affect on the threshold determination should again be quite small and less than the experimental uncertainly in the measured quantities.

5. Conclusions

The kinetic energy dependence of the collision-induced dissociation of $M^+(C_6H_5OCH_3)_x$ complexes ($M^+ = Li^+$, Na^+, K^+, Rb^+, and Cs^+, $x = 1$ and 2), with Xe is examined in a guided ion beam tandem mass spectrometer. The dominant dissociation pathway observed for all complexes is loss of an intact anisole ligand. Thresholds for the primary dissociation pathway are determined after careful consideration of the effects of reactant internal energy, multiple collisions with Xe, and the lifetime of the ionic reactants (using a loose PSL TS model). Molecular parameters needed for the analysis of experimental data as well as structures and theoretical estimates of the bond dissociation energies for the $M^+(C_6H_5OCH_3)_x$ complexes are obtained from theoretical calculations performed at the MP2(full)/6-311+G(2d,2p)//B3LYP/6–31G* level. The agreement between theory and experiment is quite good in all cases except for the $Li^+(C_6H_5OCH_3)$ complex. The absolute M^+–$(C_6H_5OCH_3)$ and $(C_6H_5OCH_3)$ M^+–$(C_6H_5OCH_3)$ bond dissociation energies as well as the change in sequential $M^+(C_6H_5OCH_3)_x$ ($x = 1$–2) bond dissociation energies are observed to decrease monotonically as the size of the alkali metal ion increases from Li^+ to Cs^+. These trends are explained in terms of the electrostatic nature of the bonding, primarily an ion–quadrupole interaction, in the $M^+(C_6H_5OCH_3)_x$ complexes and the changes in magnitude of the repulsive ligand–ligand interactions in the sandwich complexes. An interesting observation is that the σ-binding and cation–π complexes of Na^+, K^+, Rb^+, and Cs^+ are calculated to be of very similar stability. Therefore, a mixture of these three conformers is probably accessed in our experiments. Because of the very small differences in the BDEs of the σ-binding and cation–π complexes of anisole, the effects on our threshold measurements should be small. Further, the thresholds measured should correspond to the BDEs of the most-weakly bound conformer present in appreciable abundance. Comparisons made to experimental BDEs of the analogous benzene, toluene, fluorobenzene, aniline, and phenol complexes reveal that the methoxy substituent leads to moderate increase in the strength of the cation–π interaction, in both the mono and sandwich complexes, to all of the alkali metal cations. This observation is in accord with the influence of the methoxy substituent on the quadrupole moment and polarizability of the ligand as compared to benzene.

Acknowledgements

This work was supported by the National Science Foundation, Grant No. 0138504.

References

[1] H.S. Choi, S.B. Suh, S.J. Cho, K.S. Kim, Proc. Natl. Acad. Sci. U.S.A. 95 (1998) 12094.
[2] G.W. Gokel, L.J. Barbour, S.L. De Wall, E.S. Meadows, Coordin. Chem. Rev. 222 (2001) 127.
[3] J.C. Ma, D.A. Dougherty, Chem. Rev. 97 (1997) 1303.
[4] G.W. Gokel, S.L. De Wall, E.S. Meadows, Eur. J. Org. Chem. (2000) 2967.
[5] D.A. Dougherty, Science 271 (1996) 163.
[6] A.M. DeVos, M. Ultsch, A.A. Kossiakoff, Science 255 (1992) 306.
[7] A. Karlin, Curr. Opin. Neurobiol. 3 (1993) 299.
[8] M.L. Raves, M. Harel, Y.P. Pang, I. Silman, A.P. Kozikowski, J.L. Sussman, Nat. Struct. Biol. 4 (1997) 57.
[9] D.A. Stauffer, A. Karlin, Biochemistry 33 (1994) 6840.
[10] J.B. Mitchell, C.L. Nandi, I.K. McDonald, J.M. Thornton, S.L. Price, J. Mol. Biol. 239 (1994) 315.
[11] W. Zhong, J.P. Gallivan, Y. Zhang, L. Li, H.A. Lester, D.A. Dougherty, Proc. Natl. Acad. Sci. U.S.A. 95 (1998) 12088.
[12] O. Donini, D.F. Weaver, J. Comput. Chem. 19 (1998) 1515.
[13] P. Hu, C. Sorensen, M.L. Gross, J. Am. Soc. Mass Spectrom. 6 (1995) 1079.
[14] Q.P. Lei, I.J. Amster, J. Am. Soc. Mass Spectrom. 7 (1996) 722.
[15] O.M. Cabarcos, C.J. Weinheimer, J.M. Lisy, J. Chem. Phys. 110 (1999) 8429.
[16] A.H. Bond, M.L. Dietz, R.D. Rodgers (Eds.), Metal–Ion Separation and Preconcentration, ACS Symposium Series 716, American Chemical Society, Washington, DC, 1999.
[17] J. Sunner, K. Nishizawa, P. Kebarle, J. Phys. Chem. 85 (1981) 1814.
[18] V. Ryzhov, R.C. Dunbar, J. Am. Chem. Soc. 121 (1999) 2259.
[19] A. Gapeev, C.-N. Yang, S.J. Klippenstein, R.C. Dunbar, J. Phys. Chem. A 104 (2000) 3246.
[20] V. Ryzhov, R.C. Dunbar, B. Cerda, C. Wesdemiotis, J. Am. Soc. Mass Spectrom. 11 (2000) 1037.
[21] A. Gapeev, R.C. Dunbar, J. Am. Chem. Soc. 123 (2000) 8360.
[22] E.S. Meadows, S.L. De Wall, L.J. Barbour, G.W. Gokel, J. Am. Chem. Soc. 123 (2000) 3092.
[23] G.W. Gokel, S.L. De Wall, E.S. Meadows, Eur. J. Org. Chem. (2000) 2967.
[24] K. Schroeter, R. Wesendrup, H. Schwarz, Eur. J. Org. Chem. (1998) 565.
[25] P.B. Armentrout, M.T. Rodgers, J. Phys. Chem. A 104 (2000) 2238.
[26] J.C. Amicangelo, P.B. Armentrout, J. Phys. Chem. A 104 (2000) 11420.
[27] H. Huang, M.T. Rodgers, J. Phys. Chem. A 106 (2002) 4277.
[28] R. Amunugama, M.T. Rodgers, J. Phys. Chem. A 106 (2002) 5529.
[29] R. Amunugama, M.T. Rodgers, J. Phys. Chem. A 106 (2002).
[30] R. Amunugama, M.T. Rodgers, Int. J. Mass. Spectrom., accepted for publication.
[31] R. Amunugama, M. T. Rodgers, J. Phys. Chem. A 106 (2002).
[32] R.L. Woodin, J.L. Beauchamp, J. Am. Chem. Soc. 100 (1978) 501.
[33] R.W. Taft, F. Anvia, J.-F. Gal, S. Walsh, M. Capon, M.C. Holmes, K. Hosn, G. Oloumi, R. Vasanwala, S. Yazdani, Pure Appl. Chem. 62 (1990) 17.
[34] B.C. Guo, J.W. Purnell, A.W. Castleman Jr., Chem. Phys. Lett. 168 (1990) 155.
[35] S.D. Zaric, D.M. Popovic, E.-W. Knapp, Chem. Eur. J. 6 (2000) 3935.
[36] S. Mecozzi, P.A. West Jr., D.A. Dougherty, J. Am. Chem. Soc. 118 (1996) 2307.
[37] J.P. Gallivan, D.A. Dougherty, Proc. Natl. Acad. Sci. U.S.A. 96 (1999) 9459.
[38] R.C. Dunbar, J. Phys. Chem. A 104 (2000) 8067.
[39] D. Feller, D.A. Dixon, J.B. Nicholas, J. Phys. Chem. A 104 (2000) 11414.
[40] S. Tsuzuki, M. Yoshida, T. Uchimaru, M. Mikami, J. Phys. Chem. A 105 (2001) 769.
[41] S.J. Lippard, J.M. Berg, Principles of Bioinorganic Chemistry, University Science Books, Mill Valley, CA, 1994.
[42] R.C. Weast, M.J. Astle (Eds.), Handbook of Chemistry and Physics, CRC Press, Florida, 1982, p. E-61.
[43] K.J. Miller, J. Am. Chem. Soc. 112 (1990) 8533.
[44] M.T. Rodgers, K.M. Ervin, P.B. Armentrout, J. Chem. Phys. 106 (1997) 4499.
[45] M.T. Rodgers, J. Phys. Chem. A 105 (2001) 2374.
[46] E. Teloy, D. Gerlich, Chem. Phys. 4 (1974) 417;
D. Gerlich, Diplomarbeit, University of Freiburg, Federal Republic of Germany, 1971;
D. Gerlich, in: C.-Y. Ng, M. Baer (Eds.), State-selected and state-to-state ion–molecule reaction dynamics, Part I: Experiment, Advances in Chemical Physics Series, vol. 82, Wiley, New York, 1992, p. 1.
[47] K.M. Ervin, P.B. Armentrout, J. Chem. Phys. 83 (1985) 166.
[48] N.F. Dalleska, K. Honma, L.S. Sunderlin, P.B. Armentrout, J. Am. Chem. Soc. 116 (1994) 3519.
[49] T.S. Beyer, D.F. Swinehart, Comm. Assoc. Compt. Machines 16 (1973) 379;
S.E. Stein, B.S. Rabinovitch, J. Chem. Phys. 58 (1973) 2438;
S.E. Stein, B.S. Rabinovitch, Chem. Phys. Lett. 49 (1977) 1883.
[50] J.A. Pople, H.B. Schlegel, K. Ragavachari, D.J. DeFrees, J.F. Binkley, M.J. Frisch, R.F. Whitesides, R.F. Hout, W.J. Hehre, Int. J. Quant. Chem. Symp. 15 (1981) 269;
D.J. DeFrees, A.D. McLean, J. Chem. Phys. 82 (1985) 333.
[51] F.A. Khan, D.C. Clemmer, R.H. Schultz, P.B. Armentrout, J. Phys. Chem. 97 (1993) 7978.
[52] W.J. Chesnavich, M.T. Bowers, J. Phys. Chem. 83 (1979) 900.
[53] N.F. Dalleska, K. Honma, P.B. Armentrout, J. Am. Chem. Soc. 115 (1993) 12125.
[54] P.B. Armentrout, J. Simons, J. Am. Chem. Soc. 114 (1992) 8627.
[55] M.J. Frisch, G.W. Trucks, H.B. Schlegel, G.E. Scuseria, M.A. Robb, J.R. Cheeseman, V.G. Zakrzewski, J.A. Montgomery Jr., R.E. Stratmann, J.C. Burant, S. Dapprich, J.M. Millam,

A.D. Daniels, K.N. Kudin, M.C. Strain, O. Farkas, J. Tomasi, V. Barone, M. Cossi, R. Cammi, B. Mennucci, C. Pomelli, C. Adamo, S. Clifford, J. Ochterski, G.A. Petersson, P.Y. Ayala, Q. Cui, K. Morokuma, D.K. Malick, A.D. Rabuck, K. Raghavachari, J.B. Foresman, J. Cioslowski, J.V. Ortiz, B.B. Stefanov, G. Liu, A. Liashenko, P. Piskorz, I. Komaromi, R. Gomperts, R.L. Martin, D.J. Fox, T. Keith, M.A. Al-Laham, C.Y. Peng, A. Nanayakkara, C. Gonzalez, M. Challacombe, P.M.W. Gill, B. Johnson, W. Chen, M.W. Wong, J.L. Andres, C. Gonzales, M. Head-Gordon, E.S. Replogle, J.A. Pople, Gaussian 98, Revision A.9, Gaussian, Inc. Pittsburgh, PA, 1998.

[56] A.D. Becke, J. Chem. Phys. 98 (1993) 5648.

[57] C. Lee, W. Yang, R.G. Parr, Phys. Rev. B 37 (1988) 785.

[58] P.J. Hay, W.R. Wadt, J. Chem. Phys. 82 (1985) 299.

[59] E.D. Glendening, D. Feller, M.A. Thompson, J. Am. Chem. Soc. 116 (1994) 10657.

[60] D. Walter, P.B. Armentrout, J. Am. Chem. Soc. 120 (1998) 3176.

[61] J.B. Foresman, ´Æ. Frisch, Exploring Chemistry with Electronic Structure Methods, 2nd ed., Gaussian, Pittsburgh, 1996, p. 64.

[62] S.F. Boys, R. Bernardi, Mol. Phys. 19 (1979) 553.

[63] F.B. Van Duijneveldt, J.G.C.N. van Duijneveldt-van de Rijt, J.H. van Lenthe, Chem. Rev. 94 (1994) 1873.

[64] M.T. Rodgers, P.B. Armentrout, J. Phys. Chem. A 101 (1997) 1238.

[65] C. Lifshitz, Adv. Mass Spectrom. 11 (1989) 113.

[66] The metal ring-centroid distance is defined as the distance from the metal atom to the central point within the aromatic ring that lies in the plane of the carbon atoms.

[67] All comparisons make use of the theoretical results for the cation–π complexes in the determination of MADs.

[68] J.H. Williams, Acc. Chem. Res. 26 (1993) 593.